Neoplasia • Vol. 3, No. 2, 2001, pp. 143–153

www.nature.com/neo

Vascular Differences Detected by MRI for Metastatic Versus Nonmetastatic Breast and Prostate Cancer Xenografts[1]

Zaver M. Bhujwalla, Dmitri Artemov, Kshama Natarajan, Ellen Ackerstaff and Meiyappan Solaiyappan

MR Oncology Section, Division of MR Research, Department of Radiology, The Johns Hopkins University School of Medicine, Baltimore, MD 21205

Abstract

Several studies have linked vascular density, identified in histologic sections, to ''metastatic risk.'' Functional information of the vasculature, not readily available from histologic sections, can be obtained with contrast-enhanced MRI to exploit for therapy or metastasis prevention. Our aims were to determine if human breast and prostate cancer xenografts preselected for differences in invasive and metastatic characteristics established correspondingly different vascular volume and permeability, quantified here with noninvasive MRI of the intravascular contrast agent albumin–GdDTPA. Tumor vascular volume and permeability of human breast and prostate cancer xenografts were characterized using MRI. Parallel studies confirmed the invasive behavior of these cell lines. Vascular endothelial growth factor (VEGF) expression in the cell lines was measured using ELISA and Western blots. Metastasis to the lungs was evaluated with spontaneous as well as experimental assay. Metastatic tumors formed vasculature with significantly higher permeability or vascular volume ($P<.05$, two-sided unpaired *t* test). The permeability profile matched VEGF expression. Within tumors, regions of high vascular volume usually exhibited low permeability whereas regions of low vascular volume exhibited high permeability. We observed that although invasion was necessary, without adequate vascularization it was not sufficient for metastasis to occur. *Neoplasia* (2001) **3,** 143–153.

Keywords: vascular MRI, metastasis, invasion, breast and prostate cancer xenografts.

Introduction

The relationship between tumor vascularization and metastasis has attracted significant interest since the initial observation in melanoma by Srivastava et al. [1] and in breast cancer by Weidner et al. [2] that the vascular density measured in histologic sections of human breast cancer was predictive of the disposition of the patient to present with metastases. This relationship has been evaluated for different types of cancers using different immunohistochemical markers such as Factor VIII, vascular endothelial growth factor (VEGF) expression, and CD34 [3]. Among the various types of cancers studied, the relationship appears to be most evident for melanoma [1], breast [2,4], and prostate [5,6] cancer although results to the contrary have also been reported in colorectal cancer [3,7].

Noninvasive high-resolution MRI of macromolecular contrast agents provides a unique means of evaluating tumor vascular volume and permeability of human tumor models transplanted in immune suppressed mice [8–10]. Because vascular volume and permeability is obtained from the same spatial regions it is also possible to investigate the spatial relationship between these two parameters. Our interest in using noninvasive MRI to investigate the relationship between vascular characteristics and metastasis was to determine if macromolecular contrast-enhanced MRI could detect significant differences in vascular characteristics of human breast and prostate cancer lines preselected for differences in metastatic outcomes. If established, such an observation would allow the development of an MRI test to provide an additional prognostic marker to evaluate breast and prostate lesions. This is of particular importance for prostate cancer because leading health centers are investigating ''watchful waiting'' as an option for prostate cancer management. Because histologic sections cannot provide functional information, our aim was also to relate the functional MRI data to histologic findings to further understand the relationship between vascularization and metastasis. For our studies we selected three well-established human breast cancer lines (MCF-7, MDA-MB-231, MDA-MB-435), one rat (MatLyLu), and two human (DU-145, PC-3) prostate cancer cell lines. Additional studies were performed to determine VEGF secreted by cells for the six tumor models examined here. Because changes in phenotype may occur for the same cells in different laboratories, we also evaluated the invasiveness of the cell lines using an MR-compatible invasion assay we have recently developed [11]. Both spontaneous and experimental metastasis assays were also performed for the six tumor models.

Address all correspondence to: Dr. Zaver M. Bhujwalla, PhD, MR Oncology Section, Division of MR Research, Department of Radiology, The Johns Hopkins University School of Medicine, Baltimore, MD 21205. E-mail: zaver@mri.jhu.edu

[1]This work was supported by USAMRMC DAMD17-96-1-6131, a grant from the Susan G. Komen Foundation, and by NCI R01 CA73850 and NCI R01 CA82337.

Received 6 November 2000; Accepted 1 December 2000.

Methods

Tumor Models and Inoculations

Human breast cancer cells were inoculated in the left upper thoracic mammary fat pad (mfp) of female severe combined immune deficient (SCID) mice. Prostate cancer cells were inoculated subcutaneously in the right flank of male SCID mice, because the surgical procedure for orthotopic implantation into the prostate would have introduced additional complications such as the proximity of a wound near the inoculum [12]. Tumor cells were inoculated in a volume of 0.05 ml Hanks balanced salt solution (HBSS, Sigma, St. Louis, MO) at a concentration of 10^6 cells/0.05 ml. Cells in culture were maintained according to the protocols and growth media described in Refs. [11,13] and had similar doubling times of the order of 17 to 24 h. The experimental protocol was approved by the Institutional Animal Care and Use Committee. All three breast cancer lines were originally derived from pleural effusions of patients with breast cancer. Because the growth of the MCF-7 line is estrogen dependent, a 17β-estradiol pellet (0.72 mg/pellet, 60-day release, Innovative Research of American, Sarasota, FL) was inserted in the right flank using a trochar needle, 1 week before inoculation of the cells. All three prostate cancer lines used were androgen independent. The DU-145 and PC-3 human prostate cancer lines were isolated from metastasis to the brain and bone. The MatLyLu rat prostate cancer cell line was originally cloned from the Dunning rat prostate cancer line and is highly invasive and metastatic for the lymph nodes and lungs [14].

Kinetics of Albumin–GdDTPA in Blood

Albumin–GdDTPA (gadolinium diethylenetriamine pentaacetic acid, molecular weight approximately 90,000) was synthesized in our laboratory based on the procedure originally described by Ogan et al. [15]. The albumin–GdDTPA complex was dialyzed thrice against a citrate buffer and thrice against deionized water to dialyze any free GdDTPA in the preparation. Each dialysis was performed overnight in a cold room maintained at 4°C using a dialysis membrane of MW 12 to 14 kDa (SPECTRA/POR 4, Cole Parmer, Niles, IL). A separate set of experiments were performed to establish the kinetics of albumin–GdDTPA in blood. In these experiments, mice were anaesthetized and both the tail vein and the common carotid artery were cannulated. Blood samples of 20 μl were obtained from the carotid before and up to 60 minutes after intravenous administration of albumin–GdDTPA (0.2 ml of 60 mg/ml albumin–GdDTPA in saline) delivered through the tail vein. Albumin–GdDTPA concentration in blood was obtained from the T_1 relaxation times of blood samples measured at 4.7 T using a special microcoil designed by V. P. Chacko (JHU), with high signal-to-noise ratio. Although in this study animals were sacrificed at the end of each imaging experiment to obtain tumors for sectioning, and therefore 0.5 ml of blood was withdrawn from the inferior vena cava, the availability of the microcoil now allows us to perform repeated measurements of vascular volume and permeability on the same animal over a period of time, because blood T_1 can be determined from a couple of drops of blood obtained from the tail vein. A comparison of T_1 values from such a sample with T_1 obtained 3 minutes later from 0.5 ml of blood from the vena cava provided almost identical values (data not shown).

Multislice MR Imaging Studies

Imaging studies were performed on a GE CSI 4.7T instrument equipped with shielded gradients. Images were obtained with a 1-cm solenoid coil placed around the tumor. A small capillary filled with water doped with GdDTPA was attached to the side of the coil to (a) serve as an intensity reference, (b) ensure that spatial registration was identical for all images and, (c) reference histologic sections with images. The tail vein of the animal was catheterized before it was placed in the magnet; a home-built catheter system using a small T-junction (T-Connectors, 1/16 in., Cole-Parmer) was devised to minimize the dead volume, which was less than 0.04 ml. Animal body temperature was maintained at 37°C by heat generated from a pad circulating with warm water.

Multislice relaxation rates (T_1^{-1}) were obtained by a saturation recovery method combined with fast T_1 SNAPSHOT-FLASH imaging (flip angle of 10°, echo time of 2 msec). Images of four to eight slices (slice thickness of 1 mm) acquired with an in-plane spatial resolution of 0.125 mm (128×128 matrix, 16-mm field of view, NS=8) were obtained for three relaxation delays (100 msec, 500 msec, and 1 second) for each of the slices. Thus T_1 maps from eight slices could be acquired within 7 minutes. An M_o map with a recovery delay of 7 seconds was acquired once at the beginning of the experiment. Images were obtained before intravenous administration of 0.2 ml of 60 mg/ml albumin–GdDTPA in saline (dose of 500 mg/kg) and repeated, starting 3 minutes after the injection, up to 32 minutes. Relaxation maps were reconstructed from data sets for three different relaxation times and the M_o data set on a pixel by pixel basis. At the end of each imaging study, the animal was sacrificed, 0.5 ml of blood was withdrawn from the inferior vena cava, and tumors were marked for referencing to the MRI images, excised, and fixed in 10% buffered formalin for sectioning and staining. The lungs of the animal were also excised and fixed in 10% buffered formalin for sectioning and staining.

Vascular volume and permeability–surface area product (PSP) maps were generated from the ratio of $\Delta(1/T_1)$ value in the tumor image to $\Delta(1/T_1)$ of blood versus time. The slope of the $\Delta(1/T_1)$ ratio versus time in each pixel was used to compute PSP, whereas the intercept of the line at zero time was used to compute vascular volume [16–18]. Thus, vascular volumes were corrected for permeability of the vessels. 3D reconstruction of MRI data was performed using our custom-built volumetric visualization software. Adjustment of transfer functions that control the voxel transparency and intensity characteristics of various structures of interest can be performed with the software to

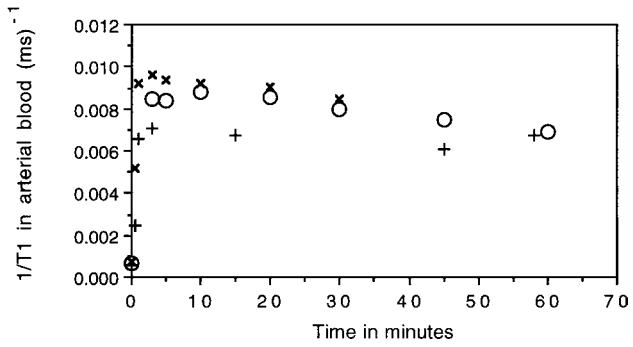

Figure 1. *Kinetics of albumin–GdDTPA in mouse blood for normal mouse (+), mouse with MDA-MB-231 tumor (○) and mouse with DU-145 tumor (×). Blood levels of albumin–GdDTPA remain constant up to 30 minutes and longer.*

delineate structures of interest from surrounding structures. The visualization software is developed around Silicon Graphics workstation systems, taking full advantage of the hardware accelerated graphics capabilities such as 2- and 3D textures to provide interactive rendering results. Furthermore, by displaying the image for each parameter through a unique color channel, e.g., vascular volume as red and vascular permeability as green, it is feasible to visually inspect the relationship between two parameters by fusing the two color maps.

Analysis of MRI Tumor Vascular Characteristics

In addition to deriving average vascular volume and permeability over the entire tumor, we separately analyzed regions of high vascular volume or high vascular permeability

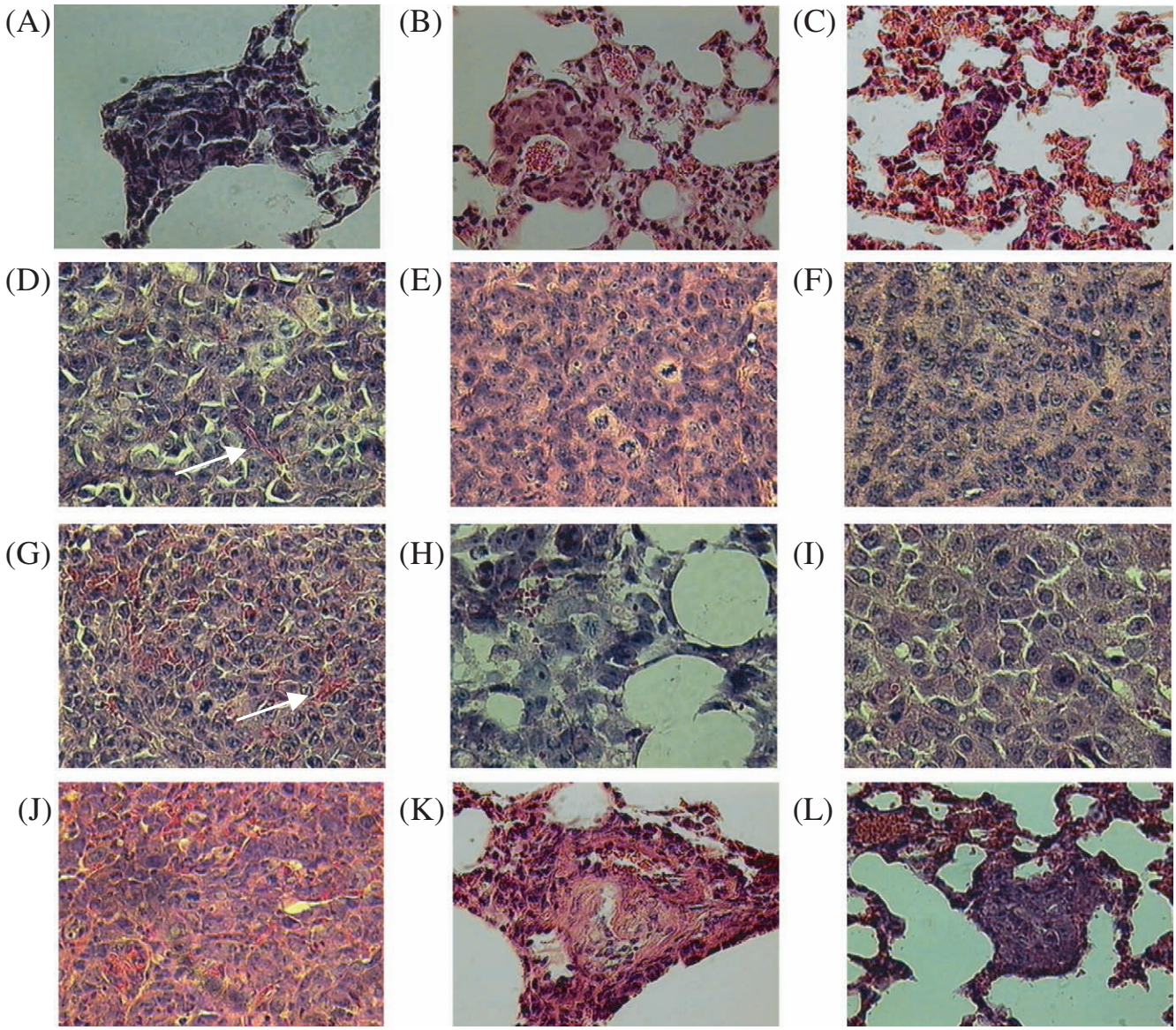

Figure 2. *High-power micrographs (×400) of 5-μm-thick histologic sections stained with hematoxylin and eosin. Sections D, E, F, G, H, and I are primary tumor sections obtained from MDA-MB-435, MDA-MB-231, MCF-7, MatLyLu, PC-3, and DU-145 tumors. Arrows indicate tumor vessels. Sections A, B, C, J, K, and L are lung sections demonstrating metastasis of MDA-MB-435 (spontaneous metastasis), MDA-MB-231 (spontaneous metastasis), MCF-7 (experimental metastasis), MatLyLu (spontaneous metastasis), PC-3 (experimental metastasis), and DU-145 (experimental metastasis) cancer cells.*

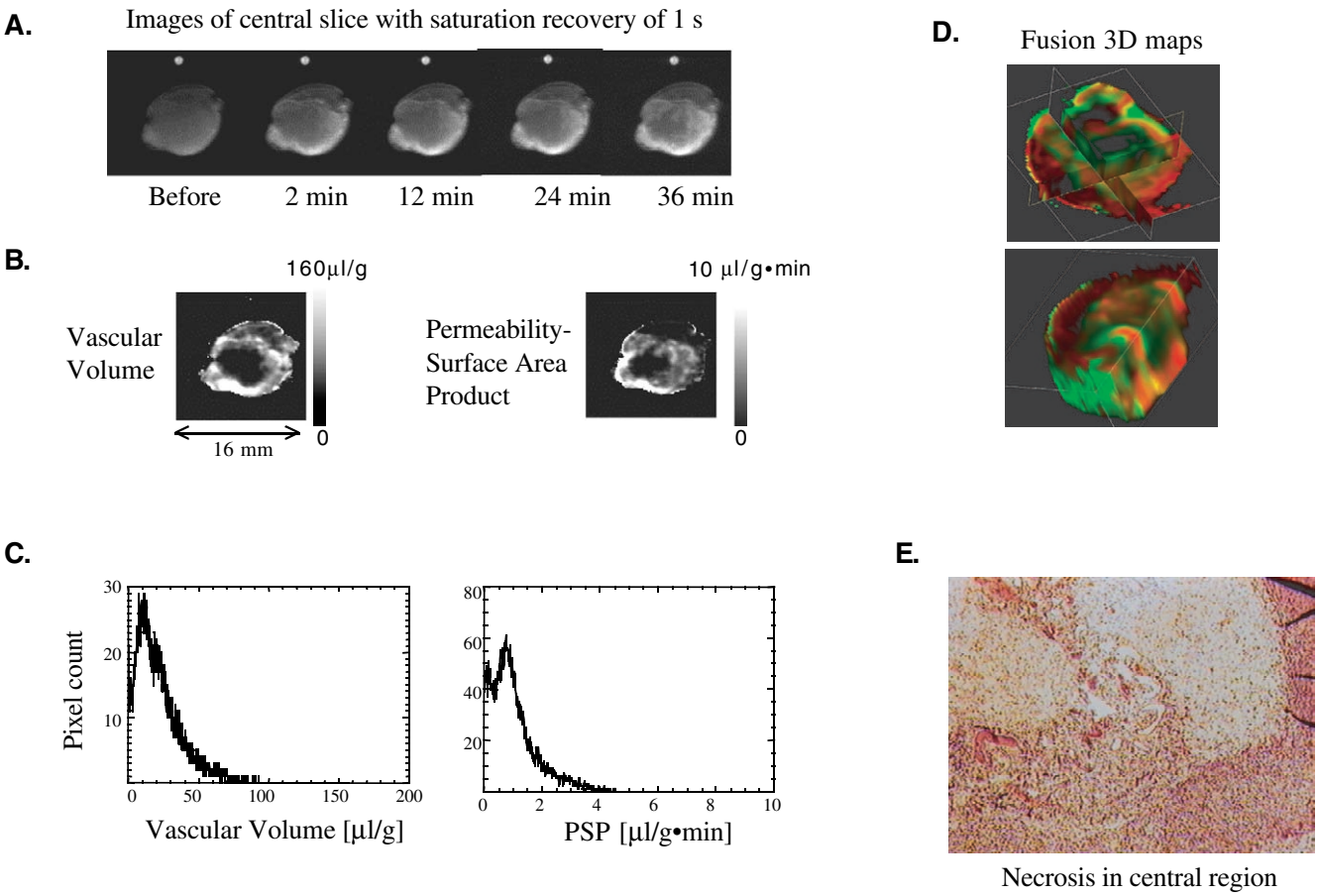

Figure 3. *(A) Raw images from a central slice of a MatLyLu tumor (180 mm^3) presented to show the actual distribution of the contrast agent; the corresponding maps of vascular volume and permeability-surface area product (PSP) are shown in (B). The frequency distribution of vascular volume and PSP for this tumor are shown in (C). 3D reconstructed fusion maps of vascular volume (red channel) and permeability (green channel) obtained from multislice data for this tumor are displayed in (D). The 3D fusion images show triplanar and volume rendered views of the fused maps. A histologic section stained with hematoxylin and eosin of the central slice of this tumor is shown in (E). Hematoxylin and eosin staining revealed necrosis and edema in the central region of this tumor.*

using a selected threshold for the highest 10% or 25% of the distribution. One reason for this approach is that the original histologic observations relating vessel density to disposition to metastasize was obtained by counting the number of vessels in the regions of high vascular density [2]. The other reason was to investigate the relationship between vascular volume and vascular permeability in regions of high vascular volume and regions of high vascular permeability. For our analyses, we therefore determined mean values of vascular volume in regions of high vascular volume as well as high permeability. Corresponding analyses were performed for permeability. In addition, the percent fractional tumor volume containing high vascular volume or high vascular permeability was also determined. Our rationale for picking two thresholds — "highest"(10%) and "high" (25%) was to ensure that we did not miss trends in the data. However, as shown subsequently, analyses of the "highest" and "high" regions provided concordant results. 3D volume data were processed with an operator independent computer program which enabled selection, mapping and display of the regions within a specified range of parameter values. For example, the vascular volume defined for the highest 10% (or 25%) values of the histogram was the median of vascular volume values for voxels within the first 10% (or 25%) of the area under the frequency distribution curve. The latter was determined by integrating the histogram, starting at the maximum value of vascular volume, with a cut off at 10% (or 25%) of the total area under the curve (see Figure 3*C*). The corresponding volume fractions of the regions were determined from the number of voxels with vascular volumes in the range defined from the histogram analysis of the data. The routine is written with IDL programming language (Research Systems, Boulder, CO) and is compatible with most operation systems.

Statistical Methods

Four to eight tumors were studied for each group. All tumors were volume matched with volumes of 200 to 300 mm^3. Statistical analyses were performed using Statview II version 1.04, 1991 (Abacus Concepts, Berkeley, CA). Statistically significant differences were established using a two-sided unpaired *t* test for 95% confidence levels or higher ($P<.05$).

Table 1. (A) Vascular Volume and (B) Permeability Data Summarized for the Six Tumor Models.

(A) Vascular Volume Data Summarized for the Six Tumor Models

Cancer Model		Highest 10% Values of Histogram ("Highest")		Highest 25% Values of Histogram ("High")		All Nonzero Values of Histogram	
Breast	Tumor Volume (mm^3)	% Volume	Mean Value ($\mu l/g$)	% Volume	Mean Value ($\mu l/g$)	% Volume	Mean Value ($\mu l/g$)
MDA-MB-435 (n=8)	212±31	8.2±0.4	67.7±12.4*	20.4±0.9	45.6±7.0*	81.3±3.6	18.4±3.1
MDA-MB-231 (n=4)	287±62	8.6±0.4	36.8±5.2	21.3±1.0	27.2±3.7	85.1±3.8	11.0±2.7
MCF-7 (n=6)	270±44	8.8±0.5	32.7±4.8	22.1±1.2	24.5±3.4	88.1±4.9	12.5±2.5
Prostate		% Volume	Value in $\mu l/g$	% Volume	Value in $\mu l/g$	% Volume	Value in $\mu l/g$
MatLyLu (n=7)	241±37	9.2±0.2†	45.4±4.9‡	23±0.6†	34.1±3.1†‡	91.3±2.4†	19.0±1.8†‡
PC-3 (n=5)	310±60	6.5±0.6‡	36.4±3.4	16.2±1.5‡	21.7±1.2‡	63.8±6.2‡	6.7±0.8‡
DU-145 (n=6)	289±49	9.0±0.2	34.0±1.7	22.5±0.5	26.4+1.1	89.5±1.8	13.1±0.6

(B) Permeability Data Summarized for the Six Tumor Models

Breast		% Volume	Mean Value ($\mu l/g \cdot min$)	% Volume	Mean Value ($\mu l/g \cdot min$)	% Volume	Mean Value ($\mu l/g \cdot min$)
MDA-MB-435 (n=8)	212±31	7.5±0.8	4.2±0.6*	19.0±2.1	2.6±0.3*	74.6±8.2	0.91±0.1*
MDA-MB-231 (n=4)	287±62	9.2±0.2*	3.5±1.1*	23.0±0.5*	2.4±0.7*	91.3±1.8*	1.24±0.4*
MCF-7 (n=6)	270±44	7.6±0.6	1.5±0.3	19.0±1.5	1.1±0.2	75.4±6.1	0.5±0.1
Prostate		% Volume	Value in $\mu l/g \cdot min$	% Volume	Value in $\mu l/g \cdot min$	% Volume	Value in $\mu l/g \cdot min$
MatLyLu (n=7)	241±37	9.2±0.1†‡	2.9±0.5†	23±0.4†‡	2.2±0.3†	91.0±1.5†‡	1.1±0.1†‡
PC-3 (n=5)	310±60	3.7±1.1‡	1.3±0.2	9.3±2.8‡	0.8±0.15	36.6±11‡	0.26±0.06‡
DU-145 (n=6)	289±49	8.0±0.3	2.1±0.5	20.0±0.8	1.5±0.3	79.1±3.3	0.6±0.1

Nonzero values and the corresponding regions represent values with detectable levels of albumin–GdDTPA where the pattern of enhancement followed the algorithm used to derive vascular volume and permeability.
Values are mean±1 SEM; n represents the number of tumors studied per model with at least four to six slices per tumor.
*Significantly different from MCF-7.
†Significantly different from PC-3.
‡Significantly different from DU-145.

Histologic Analysis of Tumors

Adjacent 5-μm-thick histologic sections obtained at 500-μm intervals through the tumor were stained with hematoxylin and eosin. Sections were digitized with a CCD camera (Sanyo, CA) attached to an optical microscope.

Assays for Spontaneous and Experimental Metastasis

Spontaneous metastasis from the cell lines was evaluated by determining the size and number of nodules in the lungs of animals sacrificed following MRI. Nodules were identified by microscopic examination of at least three 5-μm-thick lung sections stained with hematoxylin and eosin.

A separate assay was performed to evaluate experimental metastasis from these cell lines. For this assay, 2×10^6 cells were injected into the tail vein in a volume of 0.05 ml HBSS. Five animals were used for each cell line. The animals were sacrificed 2 weeks later and lung sections were examined as described before.

Assays for VEGF Expression for Cells Used in the Study

Quantitation of VEGF in conditioned media of breast cancer VEGF was measured by the Quantikine (R&D Systems, Minneapolis, MN) enzyme-linked immunosorbent assay. Cells (10^6) were seeded in a 100 mm petri dish overnight. Conditioned media from each of the cell lines were collected, centrifuged, and diluted as per manufacturer's instructions before performing the assay. The assay was repeated thrice using duplicate samples each time.

VEGF expression in prostate cell lines Because the MatLyLu cell line is not of human origin, a comparative study of VEGF expression for the three prostate cell lines was performed using Western blot analysis with a rabbit polyclonal antibody cross reactive for human, rat, and mouse VEGF (sc-507, Santa Cruz Biotechnology, Santa Cruz, CA). Serum-free RPMI-1640 was conditioned by subconfluent cultures of DU-145, PC-3, and MatLyLu for 18 hours. Ten milliliters of media was collected and concentrated to a final volume of 0.5 ml. For analysis of VEGF, the amount of conditioned medium from each cell line was normalized to cell number. The proteins in the conditioned media were resolved using both nonreducing and reducing 15% SDS-polyacrylamide gel electrophoresis [19]. The proteins were then transferred to a nitrocellulose membrane (Millipore, Bedford, MA) according to Towbin et al. [20]. After blocking in 5% skim milk, a rabbit polyclonal antibody (sc-507, Santa Cruz Biotechnology) was used to probe the membrane. The membrane was incubated with a horseradish peroxidase conjugated anti-rabbit antibody (from donkey, Amersham Pharmacia Biotech, Piscataway, NJ). The blots were developed using an enhanced chemilumi-

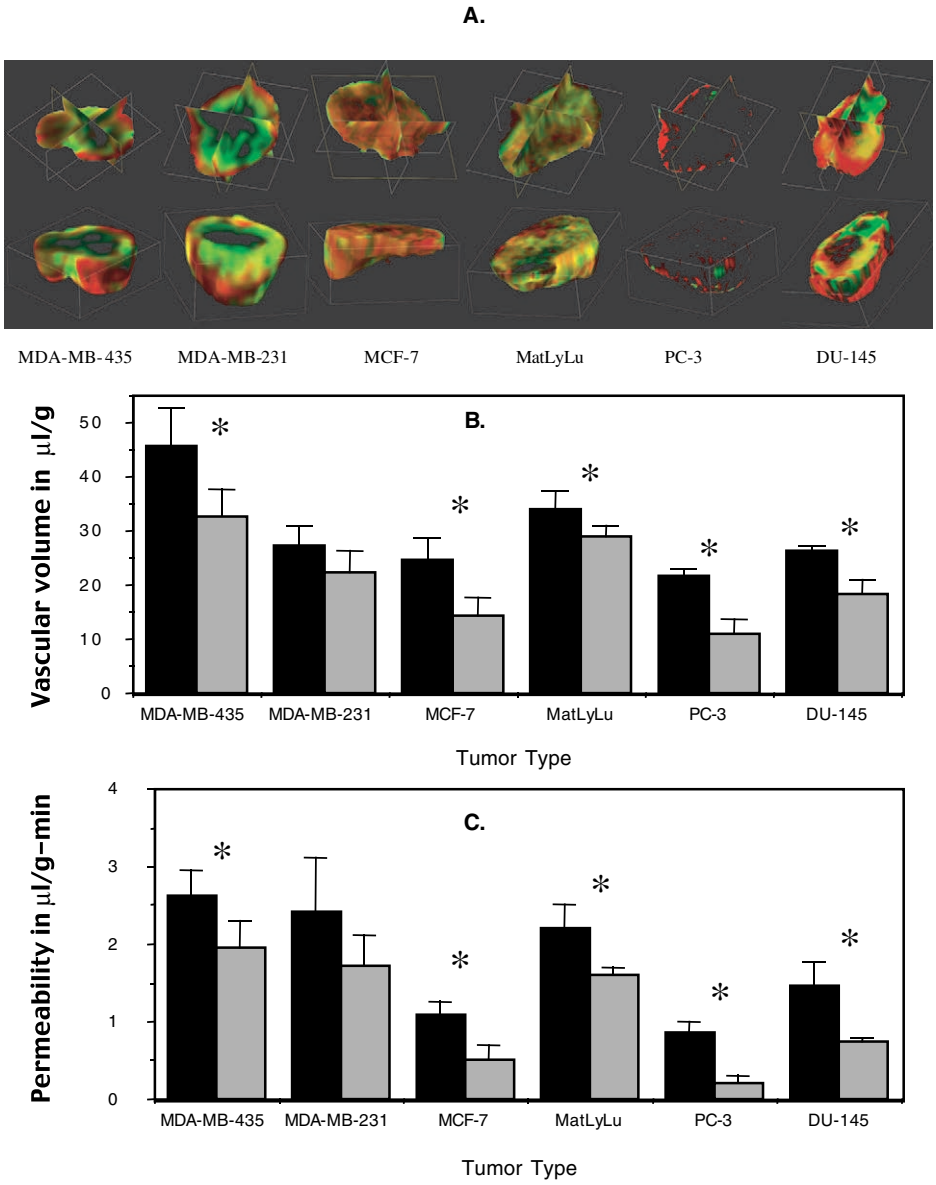

Figure 4. *Vascular volume and permeability "mismatch" characteristics of breast and prostate cancer tumor models. Representative red and green fusion maps for each of the tumor models are shown in (A); red corresponds to vascular volume, green to permeability. The mean value of the highest 25% values of vascular volume (■), and the mean vascular volumes spatially corresponding to the highest 25% values of permeability (□) are shown in (B). The mean value of the highest 25% of permeability values (■), and the permeability spatially corresponding to the highest 25% values of vascular volume (□) are shown in (C). A significant difference (P<.05) was observed for all the tumor models. The only exception to this was for the MDA-MB-231 tumor group.*

nescence (ECL-plus) system (Amersham Pharmacia Biotech) and exposed to Kodak biomax light film. Recombinant VEGF (Santa Cruz Biotechnology) was used as a standard. The intensity of VEGF staining, expressed in arbitrary units, between the prostate cell lines was quantified using NIH Image 1.62.

MRI Invasion Assays to Determine Invasive Characteristics of the Cell Lines Used in This Study

A comparison of the invasive behavior of the six cell lines used in this study was performed using our MR compatible invasion assay system. A detailed description of the assay can be found in Pilatus et al. [11]. Briefly, the assay system consists of a layer of Matrigel (Sigma) sandwiched between cells perfused under well-controlled conditions of temperature and oxygenation. The assay is stable over a period of at least 3 days and allows dynamic measurements of invasion over this time. In the study here, the assay was used to confirm previously established observations regarding the invasiveness of the six cell lines studied.

Results

The kinetics of albumin–GdDTPA over a period of time for one normal and two tumor-bearing animals are shown in

Table 2. VEGF Secretion by Cell Lines.

Tumor Model	VEGF* in pg/10^6 cells (in Culture)	Optical Density of Western Blots (in Arbitrary Units)
Breast cancer		
MDA-MB-435	161.8 ± 9.8	not determined
MDA-MB-231	422.7 ± 156	not determined
MCF-7	66.5 ± 5.0	not determined
Prostate cancer		
MatLyLu	not determined	6198
PC-3	65.0 ± 5.6	1228
DU-145	559.0 ± 49.5	4961

Characterization of VEGF in cell lines for breast cancer xenografts using ELISA or Western blotting (prostate cells only). Values for the ELISA assay represent mean ± 1 SEM from a minimum of three independent sets of cell experiments per cell line plated at separate times.

Figure 1. These data confirm previous observations that the concentration of albumin–GdDTPA remains constant in the vasculature up to at least 30 minutes. Representative histologic sections stained with hematoxylin and eosin together with lung sections demonstrating metastatic nodules for the respective tumor are shown in (Figure 2, *A* – *L*). The arrows mark blood vessels in the histologic sections that typically consist of a single layer of endothelial cells. Representative images obtained before and at four time points after intravenous administration of albumin–GdDTPA from the central slice of a multislice data set of a MatLyLu tumor, and the corresponding maps of vascular volume and permeability are shown in Figure 3, *A* and *B*. The frequency distribution of vascular volume and permeability for this tumor are displayed in Figure 3*C*. Also shown in Figure 3, are two views of 3D reconstructed red and green color fusion images of vascular volume and permeability obtained for this tumor, where spatially coincident regions of red and green should appear as yellow (Figure 3*D*). However, these fusion images exhibit very little yellow and provide visual support for our observations that spatially there is little overlap between regions of high vascular volume and high permeability. A histologic section stained with hematoxylin and eosin, obtained from the central region of this tumor, is shown in Figure 3*E*, and demonstrates that the areas of necrosis are associated with low to nondetectable vascular volume.

Data of vascular volume and permeability for the six different tumor models are summarized in Table 1(A) and (B). Volumetric analyses were performed for the highest 10% ("highest") and 25% ("high") histogram values of vascular volume and permeability as well as mean vascular volume and permeability for size-matched tumors. For the panel of breast tumor models, MDA-MB-435 demonstrated significantly higher vascular volume compared to MDA-MB-231 and MCF-7 tumors for the highest 10% and 25% analyses. This difference disappeared when analyzing values averaged over the entire tumor. For the prostate tumor models, MatLyLu tumors demonstrated significantly higher vascular volume compared to PC-3 and DU-145 tumors. Interestingly MatLyLu tumors exhibited a higher volumetric fraction in some categories as well as actual value compared to PC-3 and DU-145 tumors.

Both MDA-MB-435 and MDA-MB-231 breast tumor models were significantly more permeable in terms of mean values than MCF-7 tumors for the highest 10% and 25% analyses. In addition, volumetrically, MDA-MB-231 tumors were also significantly more permeable than MCF-7 tumors. For the prostate tumor models, MatLyLu was significantly more permeable, in terms of volumetric fraction as well as values of permeability compared to PC-3 and DU-145 tumors.

Another facet of vasculature, revealed from these analyses, was that regions of high vascular volume were not spatially coincident with regions of high permeability. These results are summarized in Figure 4. Representative red and green fusion images for the six tumor models are displayed in Figure 4*A*. The mean value of the highest 25% values of vascular volume, and the mean vascular volumes spatially corresponding to the highest 25% values of permeability are shown in Figure 4*B*. The mean value of the highest 25% of permeability, and the permeability spatially corresponding to the highest 25% values of vascular volume are shown in Figure 4*C*. A significant difference was observed for all the tumor models. The only exception to this was observed for the MDA-MB-231 tumor group. When three larger tumors of approximately 500- to 600-mm^3 volume, which were excluded from the size-matched data, were added to the MDA-MB-231 group, the mismatch for the vascular volume was significant but there was still no significant difference in permeability.

Table 3. Assays of Spontaneous and Experimental Metastasis for the Tumor Models Used in the Study.

Tumor Model	Spontaneous metastasis* (Number of Animals with Lung Nodules/Total Number of Animals Studied)	Experimental Metastasis† (Number of Animals with Lung Nodules/Total Number of Animals Studied)
Breast cancer		
MDA-MB-435	4/9	6/7
MDA-MB-231	2/7	4/6
MCF-7	0/8	1/7
Prostate cancer		
MatLyLu	2/8	4/5
PC-3	0/6	2/5
DU-145	0/6	2/5

Characterization of spontaneous and experimental metastasis for the six tumor models used in the study. For the spontaneous metastasis assay the average time from inoculation of cancer cells to excision of tumor and lungs was approximately 5 weeks for the human breast and prostate cancer model whereas MatLyLu tumors and lungs from MatLyLu tumor-bearing animals were excised at approximately 10 days. For experimental metastasis, lungs were excised 2 weeks after injecting 10^6 cells into the tail vein.

*Average time from inoculation of cancer cells to excision of tumor and lungs was approximately 5 weeks for the breast and prostate cancer models with the exception of 10 days for the MatLyLu model.

†Lungs excised 2 weeks after injecting 10^6 cells in the tail vein.

Analyses of VEGF expression for the cell lines are presented in Table 2. In the breast tumor models, MDA-MB-231 cells secreted the highest levels of VEGF, followed by MDA-MB-435 cells. MCF-7 cells secreted the lowest amount of VEGF. In the prostate tumor models, MatLyLu cells secreted the highest levels of VEGF followed by DU-145, whereas PC-3 cells secreted low levels of VEGF.

Results from the assays of spontaneous and experimental metastasis are presented in Table 3. MDA-MB-435, MDA-MB-231, and MatLyLu tumors exhibited spontaneous metastases in their respective groups. Neither MCF-7 nor PC-3 and DU-145 tumors resulted in the formation of spontaneous metastasis. Although all six cell lines were capable of forming experimental lung metastasis, again as for the spontaneous metastasis assay, MCF-7 cells induced the fewest lung nodules followed by PC-3 and DU-145 cells.

To maintain matched tumor sizes for MRI, the average time from inoculation of primary tumors to excision of lungs was only 10 days for the MatLyLu, whereas it was of the order of 5 weeks for the human tumor xenografts. Animals bearing MatLyLu tumors in excess of 20 days frequently showed almost complete lung destruction by tumor growth. Thus MatLyLu tumors appeared to be the most lethal of the six tumor models in terms of lung metastasis.

Although our cancer cell lines were preselected for literature-established differences in invasive characteristics, the phenotypic characteristics of cell lines can vary among laboratories. We therefore performed studies to confirm the invasion patterns of the six cell lines. These data are presented in Figure 5. From these images it is apparent that the Matrigel layer is significantly degraded by MDA-MB-435, MDA-MB-231, MatLyLu and PC-3 cells, whereas in comparison neither DU-145 nor MCF-7 cells degrade the Matrigel layer. The invasion index (mean±1 SEM), determined as previously described [11], for n separate experiments at approximately 47 hours for the six cell lines was as follows: MatLyLu, 2.78±0.6 at 45.6 hours, n=6; PC-3, 2.57±0.3 at 49.3 hours, n=3; DU-145, 0.22±0.1 at 48 hours, n=5; MDA-MB-435, 2.65 at 49 hours, n=1; MDA-MB-231, 1.4±0.3 at 49.1 hours, n=2; MCF-7, 0.04±0.1 at 49.3 hours, n=2. These data demonstrate that, as anticipated, MDA-MB-435 and MDA-MB-231 cells were invasive for the breast tumor group, and MatLyLu and PC-3 cells were invasive for the prostate tumor group. Both DU-145 and MCF-7 exhibited hardly any invasiveness for this assay.

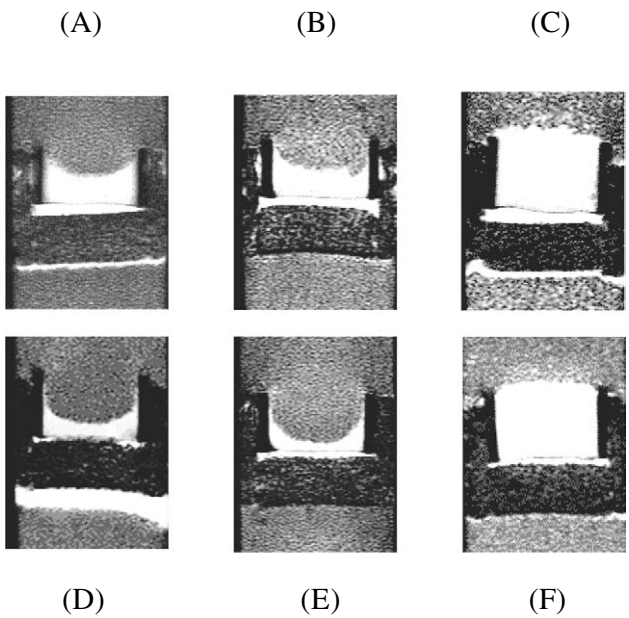

Figure 5. *(A–F): "Metabolic Boyden chamber assay" demonstrating differences in invasive characteristics of the breast (A–C) and prostate cancer (D–F) cell lines at approximately 47 hours. The T_1-weighted ^1H MR images show the bright Matrigel layer, which is significantly degraded by (A) MDA-MB-435, (B) MDA-MB-231, (D) MatLyLu, and (E) PC-3 cells, but not by the (C) MCF-7 or (F) DU-145 cells.*

Discussion

Vascular Volume and Permeability Measurements

Accurate quantitation of vascular volume and vascular permeability using the algorithm described in this study requires the assumption that the concentration of contrast agent in the blood remains constant over the time period of MRI data acquisition that was validated here. The second assumption is that water in the vascular and extravascular compartments is in fast-exchange. Data from isolated rat heart perfusion studies suggest that water exchange may be intermediate in the heart [21,22]. However, rat cardiac vessels are well organized and consist of smooth muscle cell lining as well as a layer of basement membrane, which may result in some restriction of water exchanging across the two compartments [23]. In contrast, tumor neovasculature typically consists of a single layer of endothelial cells that facilitates fast exchange. Although the assumption of fast exchange may lead to an overestimation of vascular volume by about 10%, van Dijke et al. [24] have observed a significant correlation of the order of 0.9 between vessel density and MRI-derived values of vascular volume. Other studies have also shown that vascular volume estimates made with MRI, assuming fast exchange of water, were not different from estimates made by quantifying gadolinium with atomic emission spectrsocopy [25]. Because of the noninvasive nature of MRI the technique is able to measure vascular volume corrected for permeability. With invasive techniques some leakage of the tracer will occur in highly permeable regions as soon as the tracer enters the circulation, which might lead to overestimation of values [26]. However, although measurements of vascular volume and permeability for the six tumor models used here have not been performed previously using either MRI or other techniques, the values of vascular volume and permeability obtained here are in reasonably good agreement with values for other solid tumors cited in literature obtained with traditional invasive methods [16,26–28].

Relationship between Vascular Volume and Permeability, and Necrosis

A comparison of histologic sections obtained from the imaged tumors consistently showed that areas of cell death and necrosis were typically associated with low or non-detectable vascular volume, although areas of low vascular volume were not always associated with necrosis in histologic sections. Some vessels in large necrotic areas were found to contain clumps of tumor cells. These vessels were surrounded by dead cells suggesting this as one of the mechanisms for vascular collapse in highly metastatic tumors.

We also consistently observed that regions with high vascular volume were significantly less permeable when compared with regions of high permeability within the tumors. Similarly regions of high permeability consistently exhibited lower vascular volumes. One explanation for these observations is that regions of low vascular volume are the most hypoxic and therefore will express higher VEGF [29]. This is consistent with previous observations that more intense VEGF staining is detected around areas of necrosis [30–32] where the vessels are also most permeable [17,33]. Another possible mechanism for the "mismatch" is the occurrence of lymphatic drainage, which is currently under investigation in our laboratory. These findings do imply that in addition to previously proposed mechanisms of high tumor interstitial pressure [34,35], the delivery of macromolecular agents to the tumor interstitium may also be limited by the lower permeability of tumor vasculature in precisely those viable vascular areas where they necessarily should be delivered for effective treatment.

Vascular Characteristics and VEGF Expression

The patterns of VEGF expression obtained for the cell lines were in agreement with previously published values of VEGF levels for DU-145, PC-3 [36], MCF-7, and MDA-MB-231 cells [37]. Not surprisingly, VEGF expression, rather than vascular volume, by the cells was most closely related to the permeability measured in the solid tumors. Within the breast and prostate tumor groups, the two cell lines with the lowest expression of VEGF, MCF-7 and PC-3, displayed low permeability whereas the cell lines with the highest expression of VEGF, MDA-MB-231 and MatLyLu, exhibited the highest permeability. MDA-MB-231 was also the only tumor model where the permeability in regions of high vascular volume was not significantly different from regions of low vascular volume. It is apparent, however, that the actual levels of VEGF do not relate to permeability when both breast and prostate tumor models are combined for comparison. This may be related to differences in the site of inoculation, i.e., mammary fat pad versus flank or secretion of other factors that may inhibit or reduce the effect of VEGF [38,39].

Invasion, Metastasis, and Vascularization

These experiments were designed to determine the vascular characteristics of breast and prostate cancer models preselected for differences in invasive and metastatic behavior. To determine the ability of MRI to predict the disposition of the tumor to metastasize, the experimental protocol would have required excising the tumor and allowing the animal to survive surgery and determining the metastasis in lungs and other organs at time of natural death. To justify such a protocol an initial study was required to demonstrate significant differences between vascular characteristics of the selected tumor models as is demonstrated here. In the framework of this study we established that within the breast and prostate tumor model groups, tumor models that demonstrated the ability to establish pulmonary metastases to the lung from primary tumors consistently showed significantly higher permeability and, with the exception of MDA-MB-231, higher vascular volume. These data are consistent with results from Melnyk et al. [40], where inhibition of VEGF was found to prevent tumor dissemination by a mechanism that may be distinct from its effect on tumor growth.

The metastatic characteristics of the two breast lines MDA-MB-435 and MDA-MB-231 and the nonmetastatic characteristic of MCF-7 cells are consistent with previous observations [41–43]. Similarly for the prostate tumor models MatLyLu was clonally selected for invasion and metastasis [14] and in our study, it was apparent that the MatLyLu cell line was the most lethal, whereas the DU-145 and the PC-3 cell lines were comparable both in terms of spontaneous and experimental metastasis. Although PC-3 has been observed to metastasize to the lung in other studies, this has mainly occurred from surgical orthotopic implantation in the prostate [44–46]. It is possible that in the orthotopic site PC-3 can establish better vasculature despite its low level of VEGF expression. The PC-3 cell line is undoubtedly highly invasive, and is almost identical to the MatLyLu cell line in terms of its invasive index. The results from the subcutaneous implantation of PC-3 suggests that the invasive and angiogenic phenotypes may represent two distinct subsets, i.e., highly invasive behavior does not necessarily predict for high VEGF expression or high vascularization or metastasis. Results from studies with poorly invasive MCF-7 cells transfected to overexpress the angiogenic factor FGF-1 demonstrate that angiogenic capability alone does not determine the metastatic end-point [47]; our data suggest that neither does the invasive capacity. Rather, cancer cells expressing both high invasive and angiogenic capacity represent the most lethal phenotype. Our data also suggest that targeting angiogenesis may be even more effective than targeting invasion for reducing or preventing metastasis.

Acknowledgements

We gratefully acknowledge and thank Gerald Rottman for his invaluable support and for providing us with detailed descriptions for preparing albumin–GdDTPA. We thank Noriko Mori for synthesis of albumin–GdDTPA, Gary Cromwell for maintaining the cell lines and inoculating the

tumors, and Joel B. Nelson for providing us with the prostate cancer cell lines. We gratefully acknowledge useful discussions with R. J. Gillies and Joel B. Nelson.

References

[1] Srivastava A, Laidler P, Davies RP, Horgan K, and Hughes LE (1988). The prognostic significance of tumor vascularity in intermediate-thickness (0.76–4.0 mm thick) skin melanoma. A quantitative histologic study. *Am J Pathol* **133**, 419–423.

[2] Weidner N, Semple JP, Welch WR, and Folkman J (1991). Tumor angiogenesis and metastasis-correlation in invasive breast carcinoma. *N Engl J Med* **324**, 1–8.

[3] Thompson WD, Li WW, and Maragoudakis M (1999). The clinical manipulation of angiogenesis: pathology, side-effects, surprises, and opportunities with novel human therapies. *J Pathol* **187**, 503–510.

[4] Horak ER, Leek R, Klenk N, LeJeune S, Smith K, Stuart N, Greenall M, Stepniewska K, and Harris AL (1992). Angiogenesis, assessed by platelet/endothelial cell adhesion molecule antibodies, as indicator of node metastases and survival in breast cancer. *Lancet* **340**, 1120–1124.

[5] Wakui S, Furusato M, Itoh T, Sasaki H, Akiyama A, Kinoshita I, Asano K, Tokuda T, Aizawa S, and Ushigome S (1992). Tumour angiogenesis in prostatic carcinoma with and without bone marrow metastasis: a morphometric study. *J Pathol* **168**, 257–262.

[6] Siegal JA, Yu E, and Brawer MK (1995). Topography of neovascularity in human prostate carcinoma. *Cancer* **75**, 2545–2551.

[7] Bossi P, Viale G, Lee AK, Alfano R, Coggi G, and Bosari S (1995). Angiogenesis in colorectal tumors: microvessel quantitation in adenomas and carcinomas with clinicopathological correlations. *Cancer Res* **55**, 5049–5053.

[8] Schmiedl U, Ogan M, Paajanen H, Marotti M, Crooks LE, Brito AC, and Brasch RC (1987). Albumin labeled with Gd-DTPA as an intravascular, blood pool-enhancing agent for MR imaging: biodistribution and imaging studies. *Radiology* **162**, 205–210.

[9] Schwarzbauer C, Syha J, and Haase A (1993). Quantification of regional blood volumes by rapid T1 mapping. *Magn Reson Med* **29**, 709–712.

[10] Su MY, Muhler A, Lao X, and Nalcioglu O (1998). Tumor characterization with dynamic contrast-enhanced MRI using MR contrast agents of various molecular weights. *Magn Reson Med* **39**, 259–269.

[11] Pilatus U, Ackerstaff E, Artemov D, Mori N, Gillies RJ, and Bhujwalla ZM (2000). Imaging prostate cancer invasion with multi-nuclear magnetic resonance methods: the Metabolic Boyden Chamber. *Neoplasia* **2**, 273–279.

[12] Abramovitch R, Marikovsky M, Meir G, and Neeman M (1998). Stimulation of tumour angiogenesis by proximal wounds: spatial and temporal analysis by MRI. *Br J Cancer* **77**, 440–447.

[13] Aboagye EO, and Bhujwalla ZM (1999). Malignant transformation alters membrane choline phospholipid metabolism of human mammary epithelial cells. *Cancer Res* **59**, 80–84.

[14] Isaacs JT, Isaacs WB, Feitz WF, and Scheres J (1986). Establishment and characterization of seven Dunning rat prostatic cancer cell lines and their use in developing methods for predicting metastatic abilities of prostatic cancers. *Prostate* **9**, 261–281.

[15] Ogan MD, Schmiedl U, Moseley ME, Grodd W, Paajanen H, and Brasch RC (1987). Albumin labeled with Gd-DTPA. An intravascular contrast-enhancing agent for magnetic resonance blood pool imaging: preparation and characterization [published erratum appears in *Invest Radiol* 1988 Dec;23(12):961]. *Invest Radiol* **22**, 665–671.

[16] Braunschweiger PG, and Schiffer LM (1986). Effect of dexamethasone on vascular function in RIF-1 tumors. *Cancer Res* **46**, 3299–3303.

[17] Bhujwalla ZM, Artemov D, and Glockner J (1999). Tumor angiogenesis, vascularization, and contrast-enhanced magnetic resonance imaging. *Top Magn Reson Imaging* **10**, 92–103.

[18] Ravi R, Mookerjee B, Bhujwalla ZM, Sutter CH, Artemov D, Zeng Q, Dillehay LE, Madan A, Semenza GL, and Bedi A (2000). Regulation of tumor angiogenesis by p53-induced degradation of hypoxia-inducible factor 1alpha. *Genes Dev* **14**, 34–44.

[19] Laemmli UK, Beguin F, and Gujer-Kellenberger G (1970). A factor preventing the major head protein of bacteriophage T4 from random aggregation. *J Mol Biol* **47**, 69–85.

[20] Towbin H, Staehelin T, and Gordon J (1979). Electrophoretic transfer of proteins from polyacrylamide gels to nitrocellulose sheets: procedure and some applications. *Proc Natl Acad Sci USA* **76**, 4350–4354.

[21] Donahue KM, Burstein D, Manning WJ, and Gray ML (1994). Studies of Gd-DTPA relaxivity and proton exchange rates in tissue. *Magn Reson Med* **32**, 66–76.

[22] Donahue KM, Weisskoff RM, Parmelee DJ, Callahan RJ, Wilkinson RA, Mandeville JB, and Rosen BR (1995). Dynamic Gd-DTPA enhanced MRI measurement of tissue cell volume fraction. *Magn Reson Med* **34**, 423–432.

[23] Levy BI, Duriez M, Phillipe M, Poitevin P, and Michel JB (1994). Effect of chronic dihydropyridine (isradipine) on the large arterial walls of spontaneously hypertensive rats. *Circulation* **90**, 3024–3033.

[24] van Dijke CF, Brasch RC, Roberts TP, Weidner N, Mathur A, Shames DM, Mann JS, Demsar F, Lang P, and Schwickert HC (1996). Mammary carcinoma model: correlation of macromolecular contrast-enhanced MR imaging characterizations of tumor microvasculature and histologic capillary density. *Radiology* **198**, 813–818.

[25] Okuhata Y, Brasch RC, Pham CD, Daldrup H, Wendland MF, Shames DM, and Roberts TP (1999). Tumor blood volume assays using contrast-enhanced magnetic resonance imaging: regional heterogeneity and postmortem artifacts. *J Magn Reson Imaging* **9**, 685–690.

[26] Tozer GM, and Morris CC (1990). Blood flow and blood volume in a transplanted rat fibrosarcoma: comparison with various normal tissues. *Radiother Oncol* **17**, 153–165.

[27] Peterson H-I (1979). Vascular and extravascular spaces in tumors: tumor vascular permeability. In *Tumor Blood Circulation: Angiogenesis, Vascular Morphology and Blood Flow of Experimental and Human Tumors*. H-I Peterson (Ed). CRC Press, Boca Raton. pp. 77–85.

[28] Sands H, Shah SA, and Gallagher BM (1985). Vascular volume and permeability of human and murine tumors grown in athymic mice. *Cancer Lett* **27**, 15–21.

[29] Levy AP, Levy NS, and Goldberg MA (1996). Post-transcriptional regulation of vascular endothelial growth factor by hypoxia. *J Biol Chem* **271**, 2746–2753.

[30] Shweiki D, Itin A, Soffer D, and Keshet E (1992). Vascular endothelial growth factor induced by hypoxia may mediate hypoxia-initiated angiogenesis. *Nature* **359**, 843–845.

[31] Plate KH, Breier G, Weich HA, and Risau W (1992). Vascular endothelial growth factor is a potential tumour angiogenesis factor in human gliomas *in vivo*. *Nature* **359**, 845–848.

[32] Shweiki D, Neeman M, Itin A, and Keshet E (1995). Induction of vascular endothelial growth factor expression by hypoxia and by glucose deficiency in multicell spheroids: implications for tumor angiogenesis. *Proc Natl Acad Sci USA* **92**, 768–772.

[33] Furman-Haran E, Margalit R, Grobgeld D, and Degani H (1996). Dynamic contrast-enhanced magnetic resonance imaging reveals stress-induced angiogenesis in MCF7 human breast tumors. *Proc Natl Acad Sci USA* **93**, 6247–6251.

[34] Jain RK (1987). Transport of molecules in the tumor interstitium: a review. *Cancer Res* **47**, 3039–3051.

[35] Jain RK (1987). Transport of molecules across tumor vasculature. *Cancer Metastasis Rev* **6**, 559–593.

[36] Chen HJ, Treweeke AT, Ke YQ, West DC, and Toh CH (2000). Angiogenically active vascular endothelial growth factor is over-expressed in malignant human and rat prostate carcinoma cells. *Br J Cancer* **82**, 1694–1701.

[37] Hyder SM, Murthy L, and Stancel GM (1998). Progestin regulation of vascular endothelial growth factor in human breast cancer cells. *Cancer Res* **58**, 392–395.

[38] Iruela–Arispe ML, Lombardo M, Krutzsch HC, Lawler J, and Roberts DD (1999). Inhibition of angiogenesis by thrombospondin-1 is mediated by 2 independent regions within the type 1 repeats. *Circulation* **100**, 1423–1431.

[39] Tempel C, Gilead A, and Neeman M (2000). Hyaluronic acid as an anti-angiogenic shield in the preovulatory rat follicle. *Biol Reprod* **63**, 134–140.

[40] Melnyk O, Shuman MA, and Kim KJ (1996). Vascular endothelial growth factor promotes tumor dissemination by a mechanism distinct from its effect on primary tumor growth. *Cancer Res* **56**, 921–924.

[41] Price JE, Polyzos A, Zhang RD, and Daniels LM (1990). Tumorigenicity and metastasis of human breast carcinoma cell lines in nude mice. *Cancer Res* **50**, 717–721.

[42] Thompson EW, Brunner N, Torri J, Johnson MD, Boulay V, Wright A, Lippman ME, Steeg PS, and Clarke R (1993). The invasive and metastatic properties of hormone-independent but hormone-respon-

sive variants of MCF-7 human breast cancer cells. *Clin Exp Metastasis* **11**, 15–26.

[43] Levy JA, White AC, and McGrath CM (1982). Growth and histology of a human mammary-carcinoma cell line at different sites in the athymic mouse. *Br J Cancer* **45**, 375–383.

[44] An Z, Wang X, Geller J, Moossa AR, and Hoffman RM (1998). Surgical orthotopic implantation allows high lung and lymph node metastatic expression of human prostate carcinoma cell line PC-3 in nude mice. *Prostate* **34**, 169–174.

[45] Waters DJ, Janovitz EB, and Chan TC (1995). Spontaneous metastasis of PC-3 cells in athymic mice after implantation in orthotopic or ectopic microenvironments. *Prostate* **26**, 227–234.

[46] Shevrin DH, Gorny KI, and Kukreja SC (1989). Patterns of metastasis by the human prostate cancer cell line PC-3 in athymic nude mice. *Prostate* **15**, 187–194.

[47] Zhang L, Kharbanda S, McLeskey SW, and Kern FG (1999). Overexpression of fibroblast growth factor 1 in MCF-7 breast cancer cells facilitates tumor cell dissemination but does not support the development of macrometastases in the lungs or lymph nodes. *Cancer Res* **59**, 5023–5029.